GSI

Report 2011 - 03
December

2D simulations of hohlraum targets for laser-plasma experiments and ion stopping measurements in hot plasmas

M. M. Basko, J. Maruhn, Anna Tauschwitz,
V. G. Novikov, A. S. Grushin

GSI Helmholtzzentrum für Schwerionenforschung GmbH
Planckstraße 1 · D-64291 Darmstadt · Germany
Postfach 11 05 52 · D-64220 Darmstadt · Germany

2D simulations of hohlraum targets for laser-plasma experiments and ion stopping measurements in hot plasmas

M. M. Basko
*ExtreMe Matter Institute EMMI, GSI, Darmstadt, Germany**

J. Maruhn and Anna Tauschwitz
Frankfurt University, Frankfurt

V. G. Novikov and A. S. Grushin
Keldysh Institute of Applied Mathematics, Moscow, Russia

*Electronic address: basko@itep.ru; URL: http://www.basko.net; on leave from the Alikhanov Institute for Theoretical and Experimental Physics, Moscow, Russia

Contents

1. INTRODUCTION

An attractive way to create uniform plasma states at high temperatures and densities is by using *hohlraums* — cavities with heavy-metal walls that are either directly or indirectly heated by intense laser pulses to x-ray temperatures of tens and hundreds electronvolts. A sample material, whose plasma state is to be studied, can be placed inside such a hohlraum (usually in the form of a low-density foam) and uniformly heated to a high temperature. In this case a high-Z hohlraum enclosure serves a double purpose: it prevents the hot plasma from rapid disassembly due to hydrodynamic expansion and, at the same time, suppresses its rapid radiative cooling by providing high diffusive resistivity for thermal x-rays. Of course, both the inertial and the thermal confinement of high-temperature plasmas can be achieved only for a limited period of time — on the order of nanoseconds for millimeter-scale hohlraums. Some time ago such hohlraum targets were proposed for measurements of the stopping power of hot dense plasmas for fast ions at GSI (Darmstadt) [1].

Theoretical modeling of hohlraum targets has always been a challenging task for computational physics because it should combine multidimensional hydrodynamic simulations with the solution of the spectral transfer equation for thermal radiation. In this work we report on our latest progress in this direction, namely, we present the results of 2D (two-dimensional) simulations with a newly developed radiation-hydrodynamics code RALEF-2D [2] of two types of the hohlraum targets proposed for experiments on the PHELIX laser at GSI. The first configuration is a simple spherical hohlraum with gold walls and empty interior, which has two holes — one for laser beam entrance, and the other for diagnostics. The hohlraums of this type have already been used in several experimental sessions with the NHELIX and PHELIX lasers at GSI [3]. The second type is a two-chamber cylindrical hohlraum with a characteristic Ω-shaped cross-section of the enclosure walls, whose secondary chamber is filled with a low-density foam of some low-Z sample material (carbon, plastic, etc.): it is proposed here for future ion stopping measurements. Once a high-temperature quasi-uniform plasma state is created in the low-Z sample material with the PHELIX laser beam, the beam of fast ions from the GSI UNILAC accelerator could be used to do stopping experiments in this sample plasma.

2. EMPTY SPHERICAL HOHLRAUM

A schematic view of the spherical hohlraum used in the latest experiments on the PHELIX laser is shown in Fig. 2.1. It has two circular holes along mutually perpendicular axes: one for entrance of the laser beam, and the other for diagnostic measurements of the x-ray emission from the hohlraum. This hohlraum was heated by a ~ 1 ns long frequency-doubled ($\lambda = 527$ nm) laser pulse with the total energy of $E_l \approx 130$ J. The cavity dimensions and the laser beam parameters, used in the present simulations, correspond to the March-2011 experimental campaign. The temporal laser power profile was approximated by a trapeze shown in Fig. 2.2. The transverse spatial profile of the laser intensity was approximated by the Gaussian curve with the full width at half-maximum FWHM = 0.1 mm. Below this hohlraum configuration is dubbed "the g1103 hohlraum".

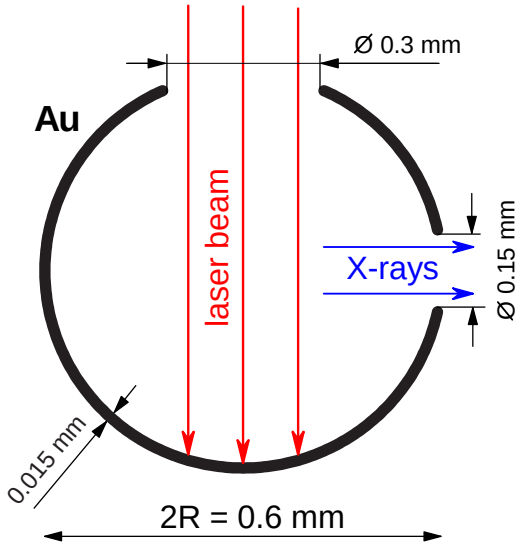

FIG. 2.1: Spherical hohlraum with two holes shot with the PHELIX laser at GSI (the g1103 hohlraum).

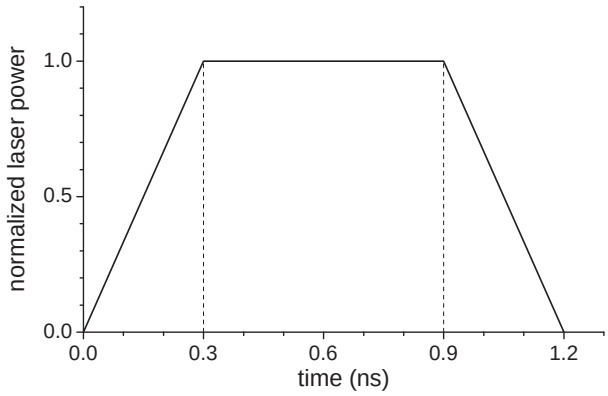

FIG. 2.2: Normalized temporal profile of the laser power used to drive the g1103 hohlraum.

2.1. Reduction to the 2D case

If a spherical hohlraum of radius R has more than one hole not along the same axis, it is already intrinsically a three-dimensional (3D) configuration. To model such a 3D hohlraum with a 2D hydro code, we have to approximate it with a suitable 2D configuration. In doing so we follow the general strategy described in the Appendix A. When applying formulae from the Appendix A, we use the notation $E \equiv E_l$ for the 3D laser pulse energy, and $\tilde{E} \equiv E_{cyl}$ for its 2D analogue.

Consider a 3D spherical hohlraum of radius R with two circular holes centered on two mutually perpendicular axes as shown in Fig. 2.3. Let the angular half-widths (as viewed from the hohlraum center) of the two holes be, respectively, θ_{eh} for the laser-entrance hole, and θ_{dh} for the diagnostics hole. The full surface area of the hohlraum sphere is $4\pi R^2$. The

combined area of the hohlraum sphere cut out by the two holes is given by

$$\begin{aligned} S_h &= 2\pi R^2 (1 - \cos\theta_{eh}) + 2\pi R^2 (1 - \cos\theta_{dh}) \\ &= 2\pi R^2 (2 - \cos\theta_{eh} - \cos\theta_{dh}) . \end{aligned} \tag{2.1}$$

Then, the remaining surface area of the physical hohlraum wall is

$$S_w = 4\pi R^2 - S_h = 2\pi R^2 (\cos\theta_{eh} + \cos\theta_{dh}) . \tag{2.2}$$

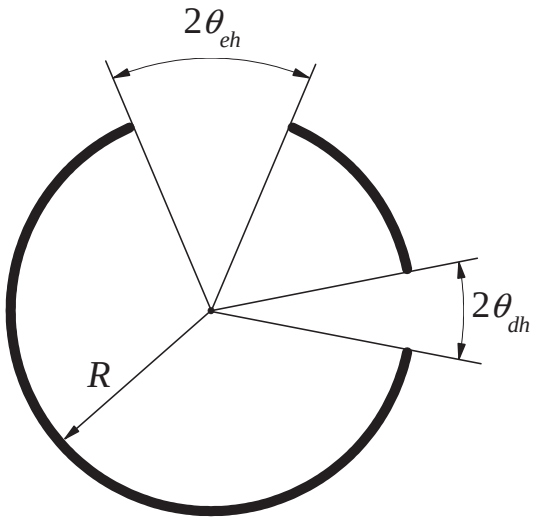

FIG. 2.3: A hohlraum of radius R with one entrance hole and one diagnostics hole.

For the present 2D simulations we approximate the original 3D hohlraum by a 2D cylindrical configuration, which extends to infinity along the z-axis perpendicular to the view plane in Figs 2.1 and 2.3; nothing depends on the thus defined z-coordinate. In the cylindrical configuration the dimensionalities of E_{cyl}, $\tilde{S}_w$, and $\tilde{S}_h$ differ from those of E_l, S_w, and S_h: E_{cyl} becomes the input energy per unit cylinder length, $\tilde{S}_w$ and $\tilde{S}_h$ are, respectively, the combined arc lengths of the hohlraum wall and of the two holes in the cylinder cross-section. In particular, we find

$$\tilde{S}_w = 2R (\pi - \theta_{eh} - \theta_{dh}) , \tag{2.3}$$

$$\tilde{S}_h = 2R (\theta_{eh} + \theta_{dh}) . \tag{2.4}$$

Then Eq. (A.4) yields

$$E_{cyl} = \frac{E_l}{R} \frac{1 + (q_{hw} - 1)(\theta_{eh} + \theta_{dh})/\pi}{2q_{hw} + (\cos\theta_{eh} + \cos\theta_{dh})(1 - q_{hw})} . \tag{2.5}$$

For the particular configuration shown in Fig. 2.1 we have

$$R = 0.3 \text{ mm}, \quad \theta_{eh} = 30^\circ, \quad \theta_{dh} = 15^\circ . \tag{2.6}$$

In the zero approximation, with $q_{hw} = 1$ we obtain

$$E_{cyl}^{(0)} = \frac{E_l}{2R} . \tag{2.7}$$

Having performed a 2D simulation with $E_{cyl} = E_{cyl}^{(0)} = 217$ J/mm, we found [from Eq. (A.7)] that $q_{hw}^{(1)} = 2.3$, which yields a first-order corrected value

$$E_{cyl}^{(1)} \approx 0.60 \, \frac{E_l}{R} = 260 \text{ J/mm}. \tag{2.8}$$

The results of simulations presented below have been obtained with this value of the laser pulse energy. For the temporal power profile of Fig. 2.2, this pulse energy corresponds to the peak irradiation intensity of 2.7×10^{14} W/cm^2.

2.2. Numerical problem setup

The hohlraum in Fig. 2.1 was simulated in the pure Eulerian mode with the 1st order in the Godunov scheme on a 9-block quasi-polar mesh with a free-float center, whose topological structure is shown in Fig. 2.4. The full range $0 \le \theta \le 2\pi$ of the polar angle θ was divided into 1440 uniform intervals (4 intervals per one degree of arc). In radial direction, the four outer blocks 6–9 were subdivided into two parts, with the inner part at 0.3 mm $\le r \le$ 0.315 mm representing the gold hohlraum wall, and the outer part at 0.315 mm $\le r \le$ 0.4 mm added as a buffer zone between the hohlraum target and the outer vacuum (see Fig. 2.5 below). The 15 μm thick hohlraum wall had 60 radial mesh intervals. The buffer zone (with 30 radial mesh intervals) is needed for adequate representation of the hydrodynamic flow around the hohlraum holes. On the total, the 2D mesh consisted of 360 000 quadrilateral cells. The boundary condition of a free outflow was applied to the outer edges of blocks 6–9.

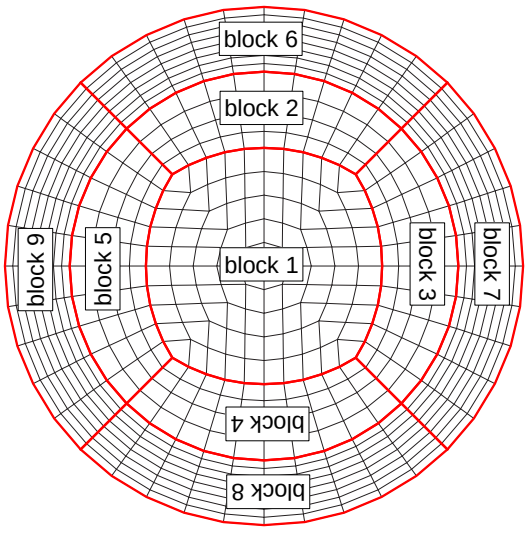

FIG. 2.4: Topological structure of the computational mesh used to simulate the g1103 hohlraum.

To be able to run the RALEF code in the purely Eulerian mode, the void interior of the hohlraum, represented by mesh blocks 1–5, was assumed to be filled with a gold vapor (same material as that of the hohlraum wall) at an initial density of $\rho_{v0} = 10^{-5}$ g/cm^3. The same vapor fill was assumed also for the outer buffer zone at 0.315 mm $\le r \le$ 0.4 mm. The initial target state was set at a pressure equilibrium between the solid and vapor states of

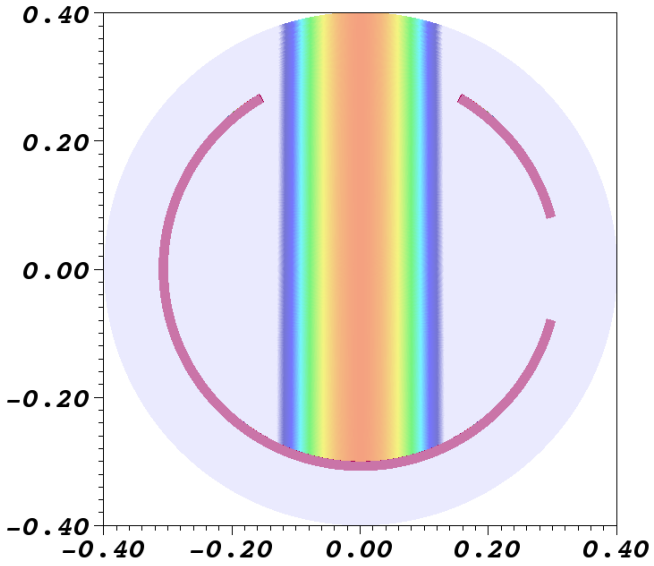

FIG. 2.5: Initial state of the computational region encompassing the g1103 hohlraum.

gold, with the initial pressure equal to $p_0 = 0.03$ bar. According to the employed equation of state, this equilibrium was achieved at the initial density $\rho_{w0} = 16$ g/cm^{3}and temperature $T_{w0} = 0.2$ eV in the solid (liquid) gold, and at the initial temperature $T_{v0} = 0.4$ eV in the gold vapor. The color view of the initial state of the entire computational region together with the incoming laser beam is shown in Fig. 2.5. Different colors in this figure represent a superposition of the density contour plot and the contour plot of the mass-specific energy deposition rate by the laser beam.

For the present simulations we used the equation of state, thermal conductivity and spectral opacities provided by the THERMOS code [4], developed at the Keldysh Institute of Applied Mathematics (Moscow). The spectral opacities have been generated by solving the Hartree-Fock-Slater equations for plasma ions under the assumption of equilibrium level population. In combination with the Planckian source function in the transfer equation, the latter means that radiation transport is treated in the approximation of local thermodynamic equilibrium (LTE).

The spectral transfer equation for thermal radiation is solved numerically for a selected number of discrete spectral groups $[\nu_j, \nu_{j+1}]$, with the original THERMOS absorption coefficients k_ν averaged inside each group j by using the Planckian weight function. Two different sets of frequency groups are prepared for each code run: the primary set with a smaller number of groups (either 1 or 7 in this case) is used at every time step in a joint loop with the hydrodynamic module, while the secondary (diagnostics) set with a larger number of groups (200 in this case) is used in the post-processor regime at selected times to generate the desired spectral output data. The 7 spectral groups of the first set had the following delimiting frequencies

$$h\nu_j = 10^{-3},\ 0.11,\ 0.2,\ 0.3,\ 0.44,\ 1.2,\ 4.0,\ 10.0\ \text{keV}; \tag{2.9}$$

The 200 groups in the second frequency set were equally spaced over the $\ln(h\nu)$ between $h\nu_1 = 10^{-3}$ keV and $h\nu_{201} = 10$ keV. An example of the spectral dependence of k_ν, provided

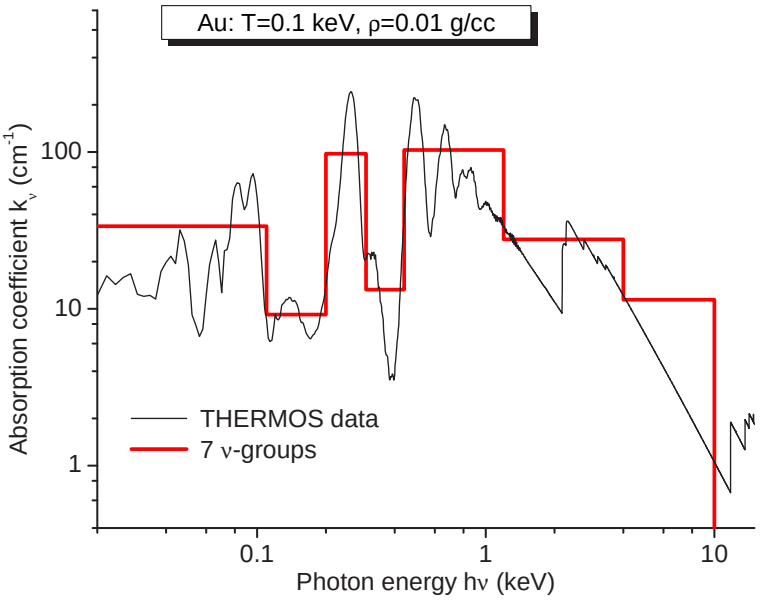

FIG. 2.6: Spectral absorption coefficient k_ν [cm^{-1}] of gold at $\rho = 0.01$ g cm^{-3}, $T = 100$ eV used in the present simulations: shown are the original data from the THERMOS code (thin black curve) together with the group-averaged values for 7 selected spectral groups (thick red curve).

by the THERMOS code for a gold plasma at $\rho = 0.01$ g cm^{-3}, $T = 100$ eV, is shown in Fig. 2.6 together with the corresponding group averages used in the RALEF simulations.

The angular dependence of the radiation intensity was calculated with the S_{12} method, which offers 168 discrete ray directions over the entire 4π solid angle.

2.3. Results of simulation

1. Overall hohlraum dynamics

The hydrodynamics and thermal history of the simulated hohlraum are illustrated in Figs. 2.7 and 2.8, where four sets of 2D contour plots for four different physical quantities are presented: each set consists of four snapshots separated by 0.3 ns in time. On these plots one sees how a plume of hot laser-ablated gold plasma rises from the bottom of the hohlraum with an average velocity of $\approx 4 \times 10^7$ cm/s. The peak temperature inside this expanding plasma cloud reaches $T \approx 0.5$ keV, the density varies in the range $\rho \approx 3 \times 10^{-4}$ – 5×10^{-3} g/cm^3, the LTE ionization degree amounts to $z_{ion} \approx 50$–60, which implies a free electron density in the range of $n_e \approx 5 \times 10^{19}$ – 10^{21} cm^{-3}. Recall that the critical electron density for a $\lambda = 527$ nm laser light is

$$n_{e,cr} = 4.01 \times 10^{21} \ \text{cm}^{-3}. \tag{2.10}$$

For $z_{ion} = 40$ the critical density of free electrons in a gold plasma corresponds to the mass density of $\rho_{cr} = 3.3 \times 10^{-2}$ g/cm^3.

The right-column frames of Fig. 2.7 demonstrate how the laser energy is absorbed. Despite the fact that by $t \approx 0.9$ ns the laser entrance hole is already filled with the ablated gold plasma, this plasma remains undercritical and the laser beam deposits its energy deep

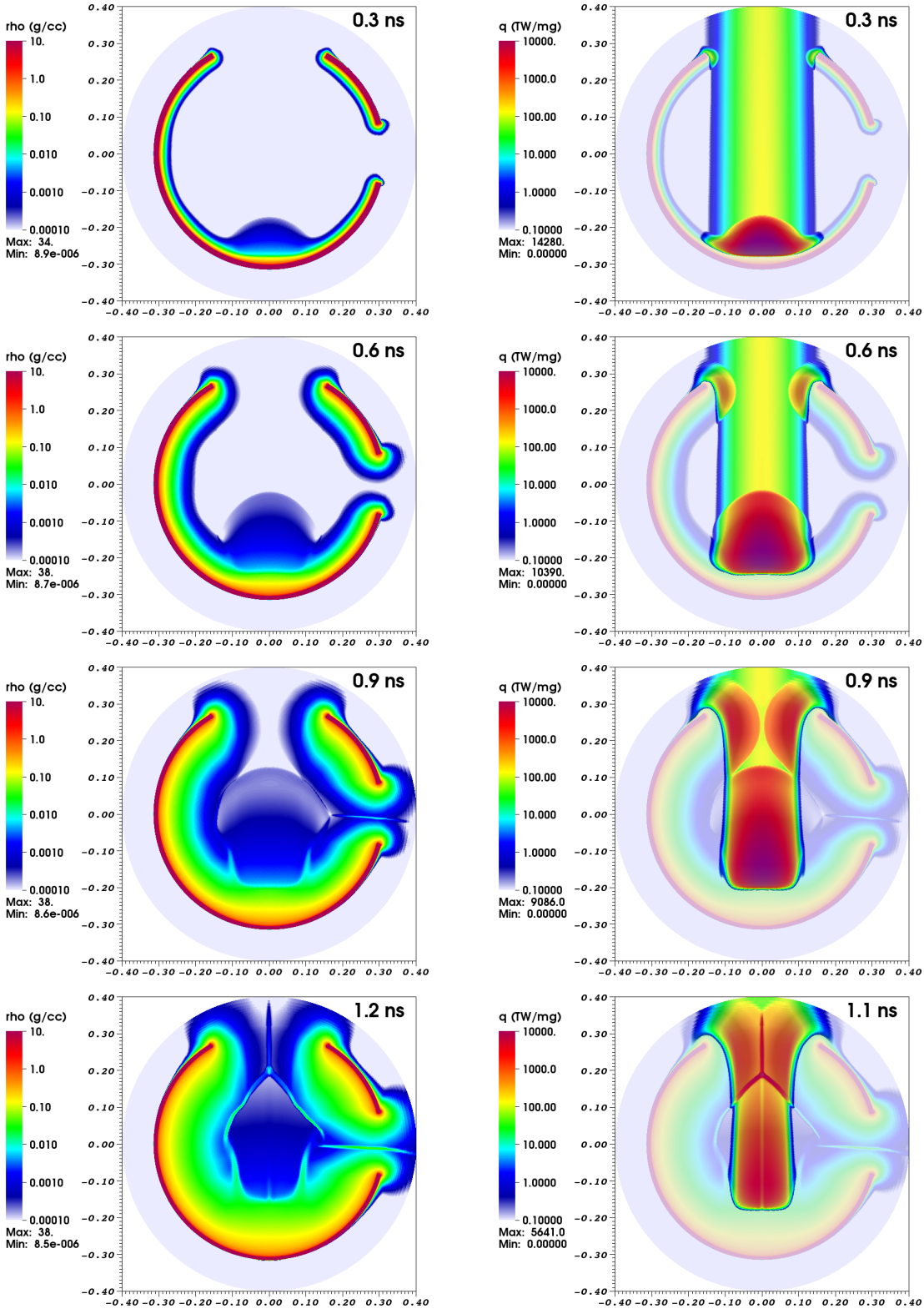

FIG. 2.7: Color contour plots of the plasma density ρ [g/cm^3] (left column), and of the mass-specific rate q [TW/mg] of the laser energy deposition (right column) in the g1103 hohlraum at four selected time moments. The last frame for the laser deposition rate q is given for $t = 1.1$ ns, i.e. 100 ps before the laser pulse ends.

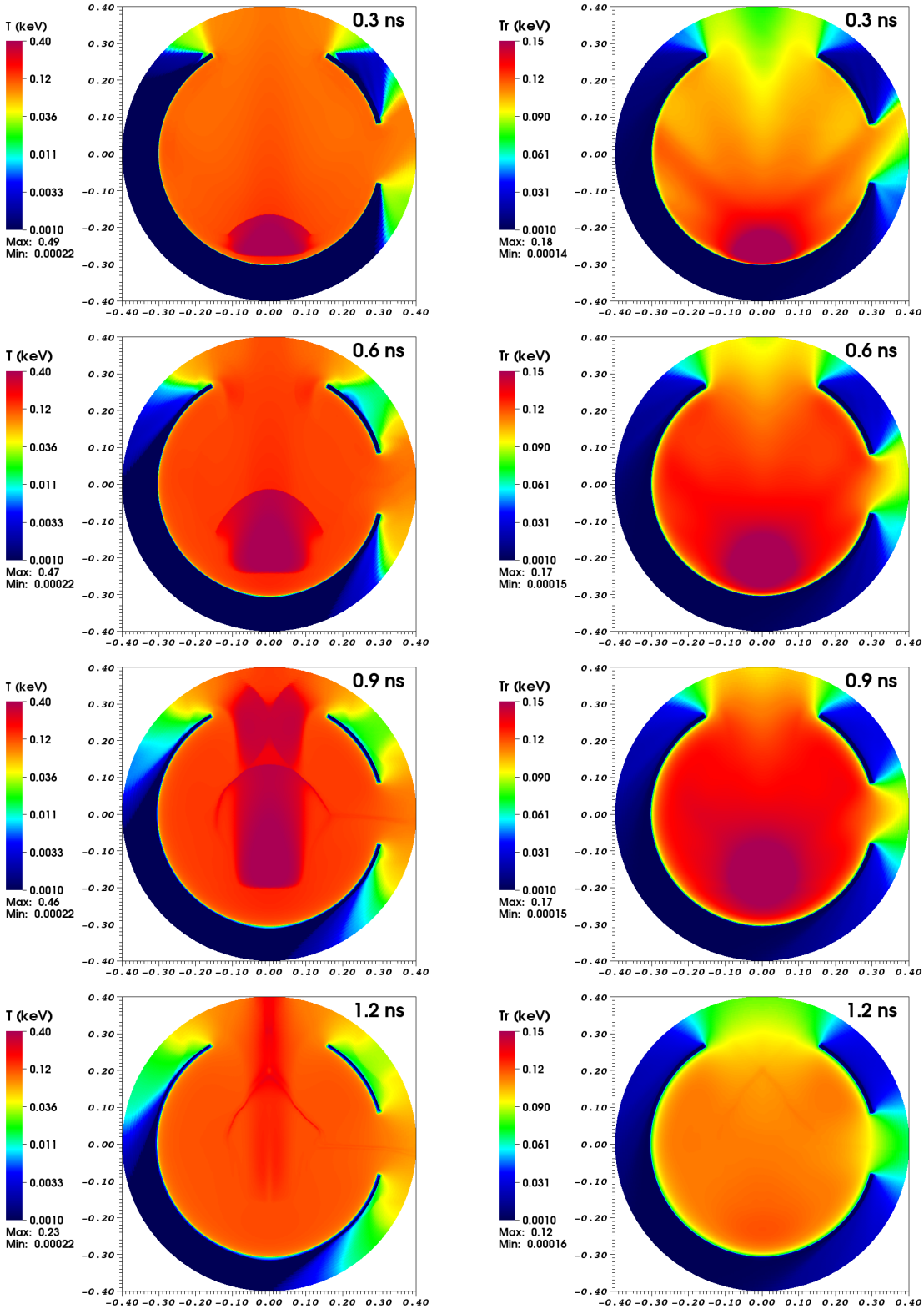

FIG. 2.8: Color contour plots of the matter temperature T [keV] (left column), and of the radiation temperature T_r [keV] (right column) in the g1103 hohlraum at four selected time moments.

inside the hohlraum cavity by the very end of the pulse at $t = 1.2$ ns. In this sense, the parameters of the laser pulse match quite well the hohlraum dynamics.

In Fig. 2.7 one sees how after $t \gtrsim 0.9$ ns the expanding clouds of the ablated plasma begin to collide with one another inside the the hohlraum. These plasma collisions lead to the formation of strongly radiating shock fronts. A characteristic feature of such radiation dominated (RD) shock fronts [5] is a practically full conversion of the kinetic energy into thermal radiation, accompanied by a very strong plasma compression. As a result, thin and dense filaments of shock compressed gold plasma are formed, which are clearly visible on the 1.2 ns density contour plot in Fig. 2.7. The density and temperature distributions across these filaments are illustrated with sample lineout plots in Fig. 2.9. A typical maximum post-shock density in the filaments reaches 0.01–0.02 g/cm^3, whereas the nearby pre-shock plasma density is 40–60 times lower. Matter temperature exhibits narrow local peaks of $T \approx 170$ eV inside the shock fronts against the background of $T \approx 120$ eV, whereas the radiation temperatures remains rather smooth; see Fig. 2.8.

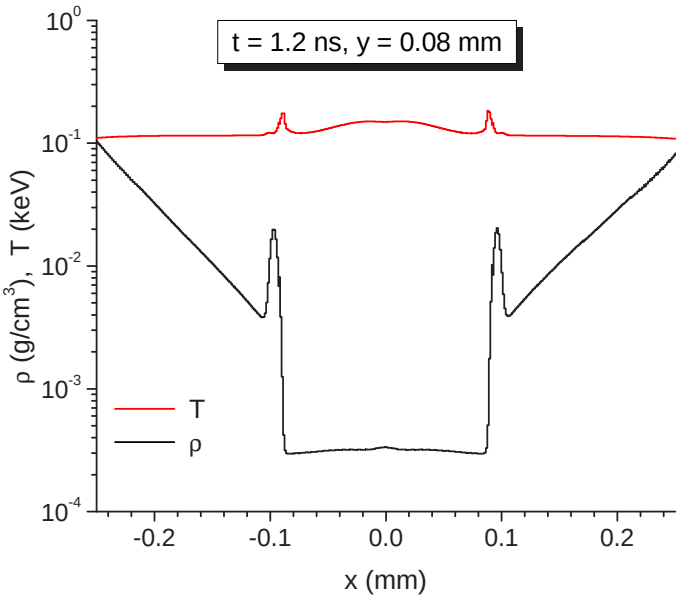

FIG. 2.9: Lineout plots of the density and matter temperature along the horizontal line (i.e. along the x-coordinate) at $y = 0.08$ mm in the central part of the g1103 hohlraum at $t = 1.2$ ns.

In Fig. 2.8 one sees that on a spatial scale of $\simeq 100\mu$m the distribution of the radiation temperature in the hohlraum is significantly non-uniform at all times when the laser is on: one observes a local maximum of $T_{r,max} \approx 170$ in the region where the laser energy is most intensely absorbed, while outside that region the radiation temperature does not exceed 130–135 eV. In addition to this physical non-uniformity, the calculated T_r distribution is affected by the so called "ray effect" — a spurious purely numerical variation inherent in the S_n method and caused by a finite number of fixed radiation propagation directions [6]. This spurious non-uniformity is clearly discernible on the $t = 0.3$ ns frame in the right-hand column of Fig. 2.8, in particular as a dip in the T_r values along the laser-beam axis near the laser-entrance hole. Also, the ray effect manifests itself as a slight angular non-uniformity in the "swelling" of the hohlraum wall on the $t = 0.3$ ns and $t = 0.6$ ns frames in the left column in Fig. 2.7.

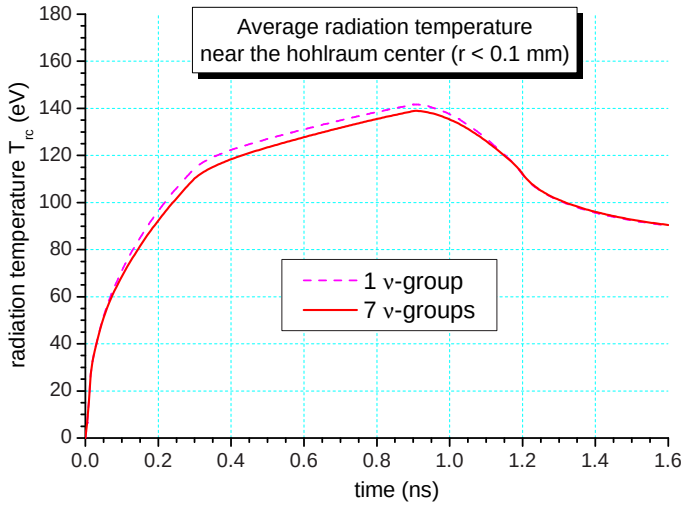

FIG. 2.10: Temporal evolution of the average radiation temperature near the center (at $r < 0.1$ mm) of the g1103 hohlraum.

Figure 2.10 shows the temporal evolution of the average value (averaged over all grid cells with a radial coordinate $r = \sqrt{x^2 + y^2} < 0.1$ mm) of the radiation temperature $T_{rc} = T_{rc}(t)$ near the center of the g1102 hohlraum. Here we compare two RALEF runs with 1 and 7 frequency groups coupled to hydrodynamics. This comparison shows that the calculated hohlraum temperature is not particularly sensitive to the number of spectral groups used. As might be expected, the peak value $T_{rp} = 139$ eV is achieved just at the end of the laser pulse $t = 0.9$ ns.

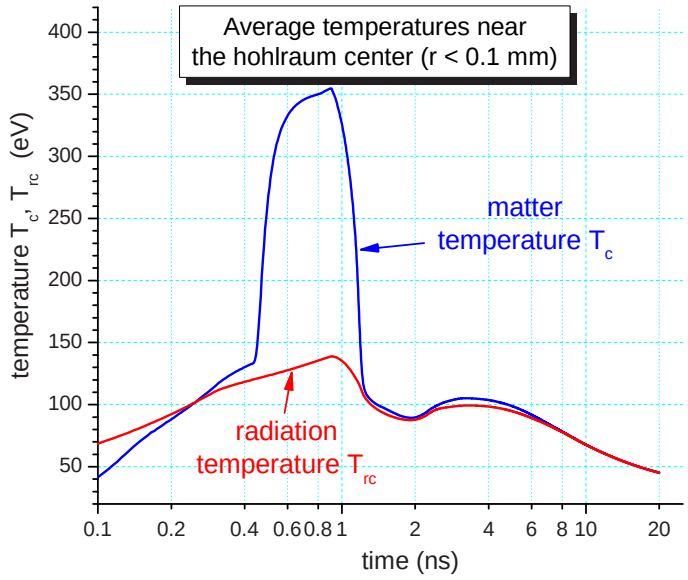

FIG. 2.11: Temporal evolution of the average matter and radiation temperatures near the center (at $r < 0.1$ mm) of the g1103 hohlraum on a long time scale.

For practical applications, of certain interest may also be the further evolution of the plasma parameters inside the hohlraum after the end of the laser pulse, as the hohlraum gradually cools down due to radiative energy loss. In Fig. 2.11 the calculated temporal behavior of both the average matter and radiation temperatures near the hohlraum center is shown for times $t \leq 20$ ns. The central matter temperature T_c was calculated by averaging over the grid-cell masses m_i,

$$T_c = \frac{\sum\limits_{r<0.1\text{mm}} m_i T_i}{\sum\limits_{r<0.1\text{mm}} m_i}, \tag{2.11}$$

in the central region $r = \sqrt{x^2 + y^2} < 0.1$ mm. A sharp rise of the matter temperature T_c at $t \gtrsim 0.5$ ns is explained by the arrival of the hot laser ablated plasma to the hohlraum center.

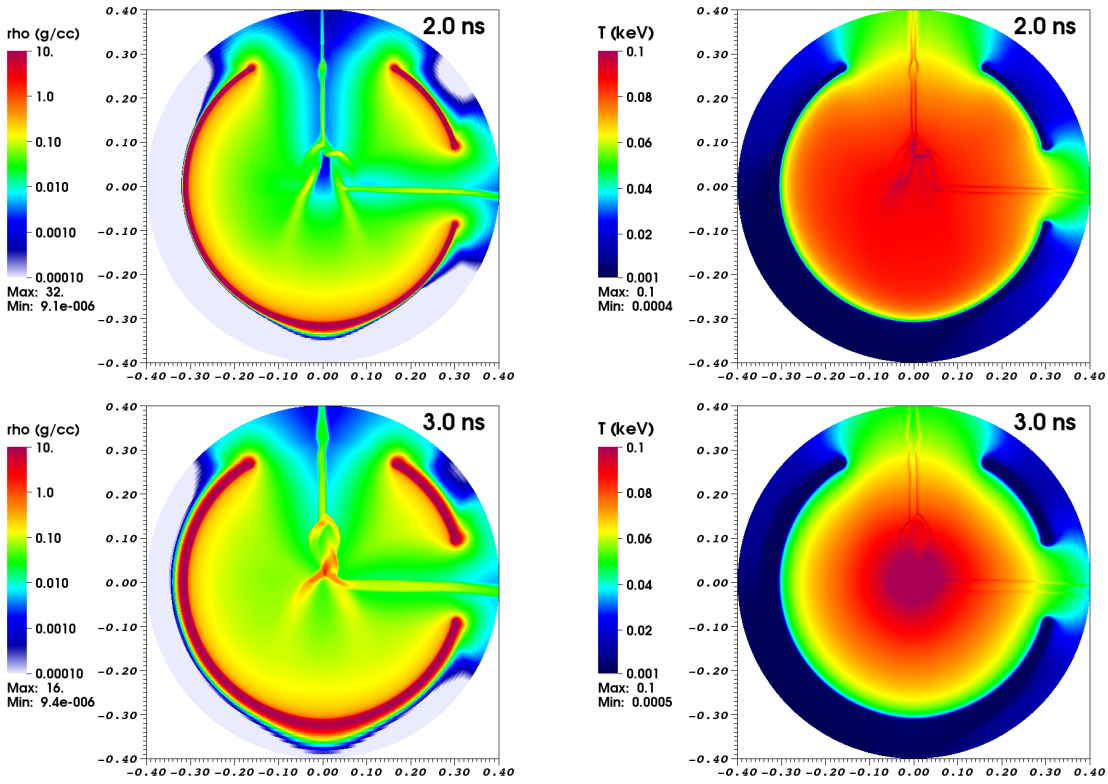

FIG. 2.12: Color contour plots of the plasma density ρ [g/cm^3] (left column), and of the plasma temperature T [eV] (right column) in the g1103 hohlraum at $t = 2$ ns and 3 ns.

After the laser pulse is turned off at $t = 1.2$ ns, the radiation and matter temperatures rapidly come to a close equilibrium, and the hohlraum begins to cool down as a whole. At $t = 2$–4 ns, however, the central region of the hohlraum is reheated to a temperature $T_c \approx T_{rc} \approx 100$ eV. This secondary reheating is caused by the convergence of the hydrodynamic flow towards the center. Indeed, as one can infer from Fig. 2.9, a steep average radial gradient of plasma pressure is established by $t = 1.2$ ns, which sweeps the ablated gold plasma towards the hohlraum center. This radiation-induced plasma flow converges upon the center at $t \approx 2.1$ ns, and, as a result, by $t \approx 3$ ns a hot central spot with radius

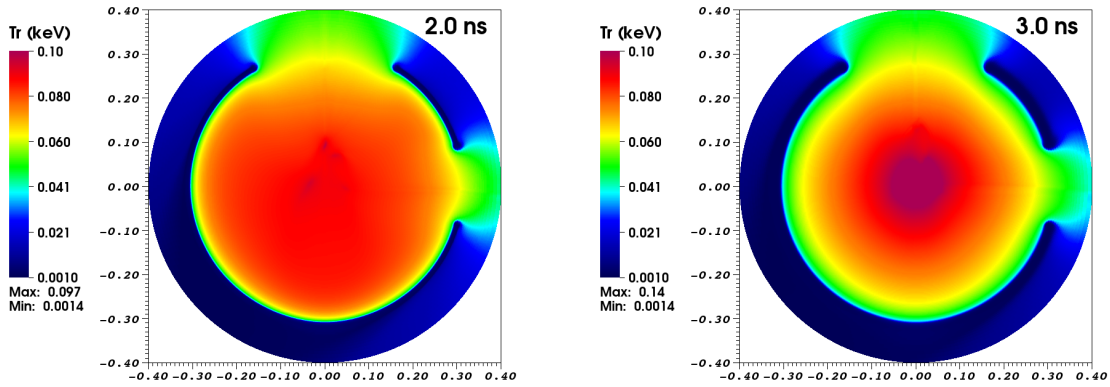

FIG. 2.13: Color contour plots of the radiation temperature T_r [eV] in the g1103 hohlraum at $t = 2$ ns and 3 ns.

$r \approx 0.1$ mm is formed — as it is clearly seen in the color contour plots of Figs. 2.12 and 2.13. After that the phase of gradual cooling on a time scale of 10–20 ns sets in.

2. Calculated x-ray spectra

Figure 2.14 shows the three calculated x-ray spectra that should be observed through the 0.15-mm wide diagnostic hole of the hohlraum (see Fig. 2.3) at $t = 0.4$ ns, 0.7 ns and 0.9 ns. Plotted in this figure is the spectral power F_ν [TW mm^{-1} sr^{-1}] per unit cylinder length, obtained by integrating the spectral intensity I_ν along an imaginary observation slit (perpendicular to the x-axis) over the range -0.1 mm $< y < +0.1$ mm.

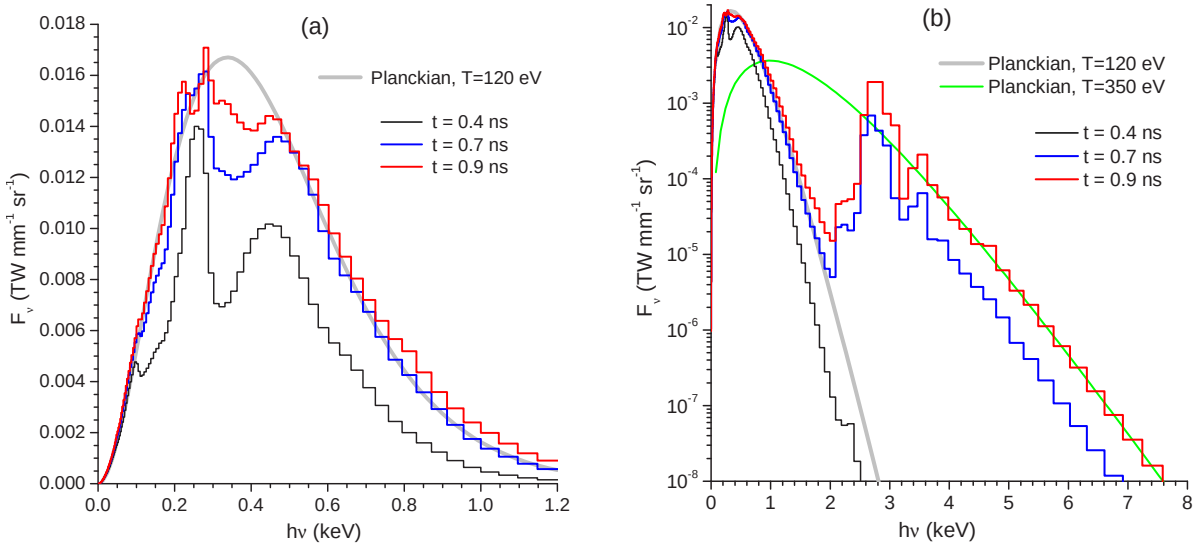

FIG. 2.14: Calculated x-ray spectra as would have been observed through the diagnostic hole at three time moments, $t = 0.4$ ns, 0.7 ns and 0.9 ns. Two different representations of the same spectra highlight (a) the soft part and (b) the hard component of the calculated spectra.

If we try to fit the main (soft) part of the x-ray spectrum at $h\nu \lesssim 2$ keV with a Planckian curve, we obtain the values $T_P = 100$ eV, 120 eV and 130 eV of the Planckian-fit temperature T_P for times $t = 0.4$ ns, 0.7 ns and 0.9 ns, respectively. However, as one sees from Fig. 2.14a, the calculated spectra exhibit significant deviations from the smooth Planckian curves near the emission maxima, especially at earlier times $t \lesssim 0.5$ ns.

A salient feature in Fig. 2.14b is the emergence of a strong hard x-ray component at $h\nu \gtrsim 3$ keV for times $t > 0.5$ ns. This extra hard emission originates from the hot ($T \approx 0.3$–0.5 keV) laser-ablated plasma cloud rising from the bottom of the hohlraum. By $t \approx 0.5$ ns this cloud reaches the hohlraum center and becomes visible through the diagnostic hole; see Figs. 2.7 and 2.8. As might be expected, the spectral slope of the hard component can be approximated by Planckian curves with fit temperatures T_P close to the plasma temperatures in the rising hot cloud, in particular, $T_P = 0.35$ keV for $t = 0.9$ ns.

3. Hohlraum temperature scaling

For practical applications it is important to know the scaling of the hohlraum temperature T_r with the input laser energy E (E_{cyl} in the cylindrical geometry). Figure 2.15 shows four values of the peak radiation temperature T_{rp}, calculated with the RALEF code for four different laser pulse energies, varying from a quarter to two times the nominal value of $E_{cyl} = 260$ J/mm. The hohlraum configuration and dimensions in these four runs were kept fixed; T_{rp} is defined as the temporal maximum (occurring always near $t = 0.9$ ns) of the central radiation temperature $T_{rc} = T_{rc}(t)$ (shown in Fig. 2.10), obtained by averaging the T_r values over the grid cells in the central region $r = \sqrt{x^2 + y^2} < 0.1$ mm. The calculated scaling can to a good accuracy be approximated by a power law

$$T_{rp} = 139 \left(\frac{E_{cyl}}{260 \text{ J/mm}} \right)^{0.31} \text{ eV}. \tag{2.12}$$

The scaling (2.12) can be easily explained in terms of a non-linear heat wave propagating into a quasi-static gold wall. The laser energy E deposited inside the hohlraum is mainly spent to heat up the inner hohlraum wall to a certain temperature $T = T_r$ by the mechanism of radiation heat conduction (matter and radiation temperatures inside a dense high-Z hohlraum wall are practically the same under our conditions). If we ignore for simplicity the hydrodynamic motion and assume the hohlraum wall to be heated under a fixed density ρ, we can describe the process of wall heating by the equation of non-linear thermal conduction

$$\frac{\partial \mathcal{E}}{\partial t} = \frac{\partial}{\partial x} \left(\kappa \frac{\partial T}{\partial x} \right), \tag{2.13}$$

where $\mathcal{E} = \mathcal{E}(T)$ [erg/cm^3] is the volume-specific internal energy of gold at temperature T, x is the penetration depth into the hohlraum wall,

$$\kappa = \frac{16}{3} \sigma_{SB} T^3 l_R \tag{2.14}$$

is the radiative heat conduction coefficient [5], l_R is the Rosseland mean free path of thermal photons, and σ_{SB} is the Stefan-Boltzmann constant. Aiming at derivation of a simple scaling law, we assume power-law dependences

$$\mathcal{E}(T) = \mathcal{E}_* \, T^{k+1}, \quad l_R = l_* \, T^m, \tag{2.15}$$

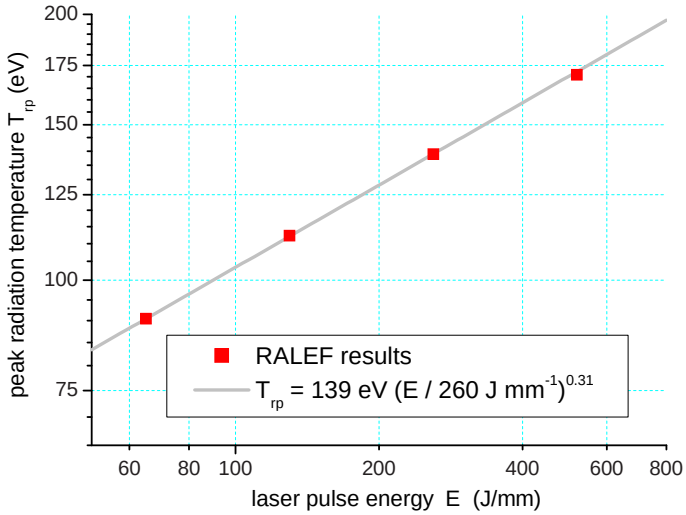

FIG. 2.15: Scaling of the peak radiation temperature T_{rp} near the hohlraum center with the laser pulse energy E. The hohlraum geometry and the functional form of the temporal laser power profile were kept fixed.

where $\mathcal{E}_*$ and l_* are some constants.

Now, if we consider a sequence of laser pulses, which have the same normalized temporal power profile and differ only in the value of the peak power (or, equivalently, in the value of the total deposited energy E), then Eq. (2.13) must be solved for a set of similar boundary conditions, with the boundary energy flux proportional to the energy fluence

$$F_w \equiv \frac{E_w}{S_w} = \frac{E}{S_w + S_h q_{hw}}, \tag{2.16}$$

i.e. to the energy absorbed by the unit surface area of the hohlraum; here S_w is the surface area of the hohlraum wall, S_h is the summed surface area of the hohlraum holes, $q_{hw} = (1-\alpha_w)^{-1}$, where $\alpha_w < 1$ is the diffusive wall albedo; for more details see Appendix A. On the other hand,

$$F_w = x_w \mathcal{E}, \tag{2.17}$$

where $\mathcal{E}$ is some characteristic value of the volume-specific internal energy in the heat wave, and x_w is the effective thickness of the heat wave.

From Eq. (2.13) one readily infers that, for a sequence of similar boundary conditions, the penetration depth x_w of the thermal wave scales as

$$x_w \propto \mathcal{E}^{(m+3-k)/(2k+2)}, \tag{2.18}$$

which implies

$$F_w \propto \mathcal{E}^{(m+k+5)/(2k+2)} \propto T^{(m+k+5)/2}, \tag{2.19}$$

or, equivalently,

$$T_r \approx T \propto \left(\frac{E}{S_w + S_h q_{hw}}\right)^{2/(m+k+5)}. \tag{2.20}$$

With the equation of state and opacities of gold, used in the present RALEF simulations, we find that $k \approx 0.6$ and $m \approx 0.8$ at $\rho \simeq 1$ g/cm^3, 70 eV $\lesssim T \lesssim$ 140 eV. Then, for fixed

values of S_w, S_h and q_{hw}, we obtain $T_r \propto E^{0.31}$ — in perfect agreement with the RALEF results displayed in Fig. 2.15.

3. CYLINDRICAL Ω-HOHLRAUM WITH A FOAM FILL

As the next step, we consider a hohlraum configuration which can accommodate a certain sample material, supposed to be uniformly heated by the quasi-thermal hohlraum radiation. Such a hohlraum must consist of at least two chambers — one (primary) for absorption of the heating laser beam, the other (secondary) containing the sample material — because the laser radiation cannot be allowed to directly interact with the sample material. We assume that the secondary chamber has the same size and shape as the empty spherical (cylindrical) hohlraum investigated in the previous section. This secondary chamber must now be heated by quasi-thermal x-rays, generated in the primary absorption chamber. To avoid excessive energy losses into the enclosure walls and the laser-entrance hole, the absorption chamber should have (i) an as small as possible total area of the walls, combined with (ii) an as wide as possible opening into the secondary chamber, and (iii) an as narrow as possible laser-entrance hole.

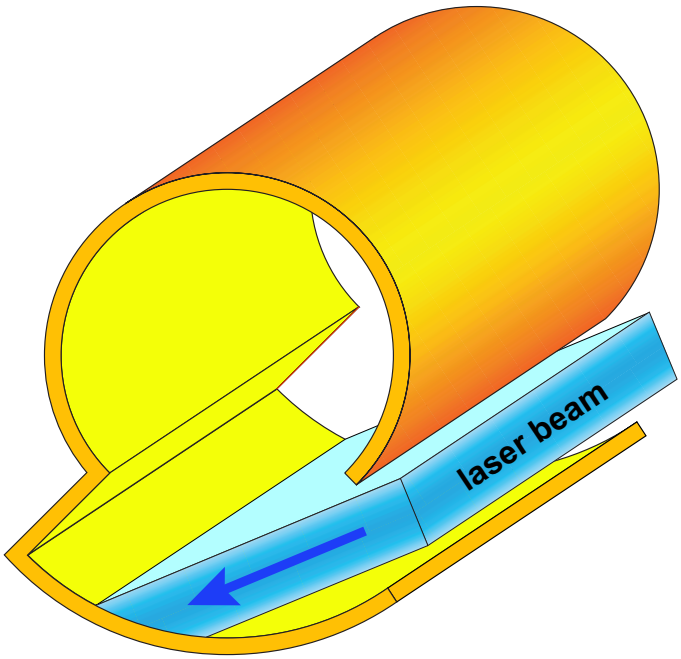

FIG. 3.16: General 3D view of an empty cylindrical Ω-hohlraum.

A 3D view of a two-chamber cylindrical hohlraum that should roughly satisfy these requirements is shown in Fig. 3.16. Here from the very beginning we consider a cylindrical configuration, keeping in mind possible experiments with the beams of fast ions which would propagate along the direction of the cylinder axis. Because the cross-section of the hohlraum wall slightly resembles the Greek letter Ω, we dubbed it "the Ω-hohlraum". The main goal of the simulations, presented below, was to demonstrate that quasi-uniform plasma states with temperatures close to $T = 100$ eV — sufficient to practically fully ionize carbon atoms — could be created with laser input energies around 100 J/mm.

3.1. The hohlraum and the laser beam parameters

The dimensions of the simulated Ω-hohlraum are given in Fig. 3.17, its actual initial configuration — in Figs. 3.18 and 3.22. Similar to the previous case, this hohlraum is assumed to be heated by a frequency-doubled ($\lambda = 527$ nm) PHELIX laser pulse with the normalized temporal power profile shown in Fig. 2.2. The total energy of the laser pulse was fixed at $E_{cyl} = 100$ J/mm. Conforming to the target geometry, a cylindrical laser focal spot was assumed with a FWHM = 0.05 mm Gaussian profile in the transverse (i.e. perpendicular to the laser beam axis in the cross-section view) direction. The relative orientation of the laser beam with respect to the Ω-hohlraum is indicated in Figs. 3.16–3.18 and 3.22.

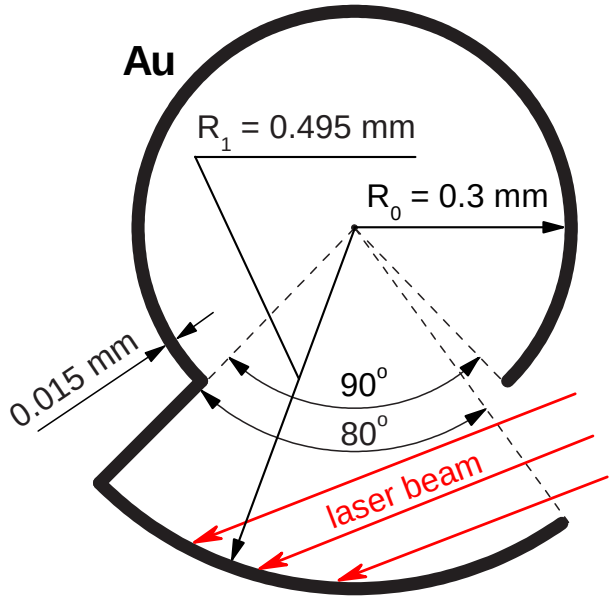

FIG. 3.17: Principal dimensions of the simulated Ω-hohlraum.

3.2. Simulation results for an empty Ω-hohlraum

For a better assessment of the potential capabilities of the Ω-hohlraum for generating high-temperature states of sample plasmas, we begin by simulating an empty Ω-hohlraum without the sample material in its secondary chamber.

1. Numerical problem setup

Similar to the g1103 hohlraum, the empty Ω-hohlraum was simulated in the pure Eulerian mode with the 1st order Godunov method on a 13-block quasi-polar mesh with a free-float center. The mesh had the same structure as shown in Fig. 2.4, except that an extra circular layer of 4 blocks was added to accommodate the absorption chamber (block 12) and the outer buffer zone (blocks 10, 11, and 13). The $0 \le \theta \le 2\pi$ range of the polar angle θ was divided into 720 uniform intervals (2 intervals per one degree of arc). On the total, the 2D

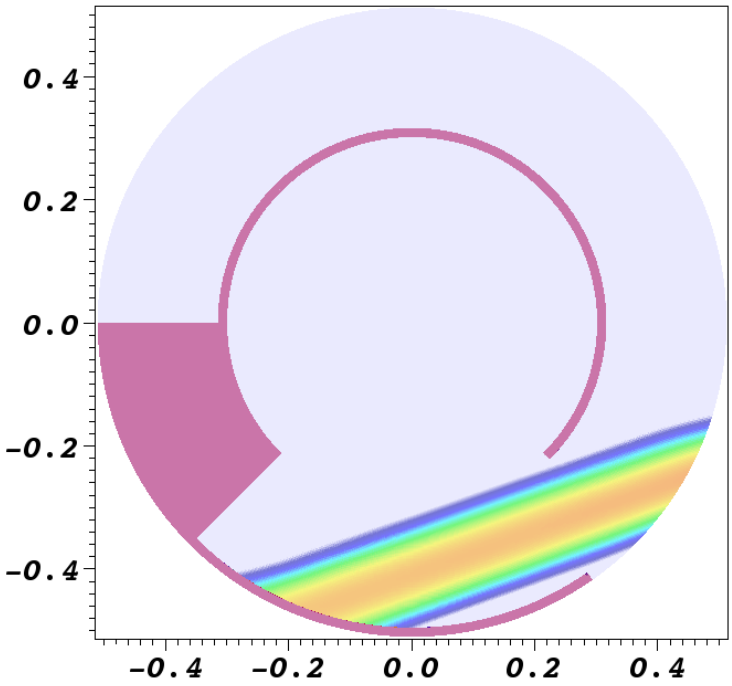

FIG. 3.18: Initial state of the computational region encompassing the empty Ω-hohlraum.

mesh consisted of 239 600 quadrilateral cells. The boundary condition of a free outflow was applied to the outer edges of blocks 10–13.

The void interior of both the primary and the secondary hohlraum chambers was assumed to be filled with a gold vapor (same material as that of the hohlraum wall) at an initial density of $\rho_{v1} = 10^{-4}$ g/cm^3. The vapor fill of the outer buffer zone had the initial density of $\rho_{v0} = 10^{-5}$ g/cm^3. The initial target state was set at a pressure equilibrium between the solid and vapor states of gold, with the initial pressure equal to $p_0 = 1$ bar. According to the used equation of state, this equilibrium was achieved at the initial density $\rho_{w0} = 18$ g/cm^3 and temperature $T_{w0} = 0.24$ eV in the solid (liquid) gold, and at the initial temperatures $T_{v0} = 4.26$ eV and $T_{v1} = 1.12$ eV in the gold vapor. The color view of the initial state of the entire computational region together with the incoming laser beam is shown in Fig. 3.18. Different colors in this figure represent a superposition of the density contour plot and the contour plot of the mass-specific energy deposition rate by the laser beam.

Radiation transport coupled to hydrodynamics was simulated by using the S_{12} angular quadrature and practically the same 7 frequency groups,

$$h\nu_j = 10^{-4},\ 0.11,\ 0.2,\ 0.3,\ 0.44,\ 1.2,\ 4.0,\ 20.0\ \text{keV}, \tag{3.21}$$

as for the g1103 hohlraum [cf. Eq. (2.9)].

2. Results of simulation

The plasma dynamics and the temperature evolution in the simulated empty Ω-hohlraum are illustrated in Figs. 3.19 and 3.20, where four sets of 2D contour plots for four different physical quantities are presented: each set consists of two snapshots in the middle ($t = 0.6$ ns)

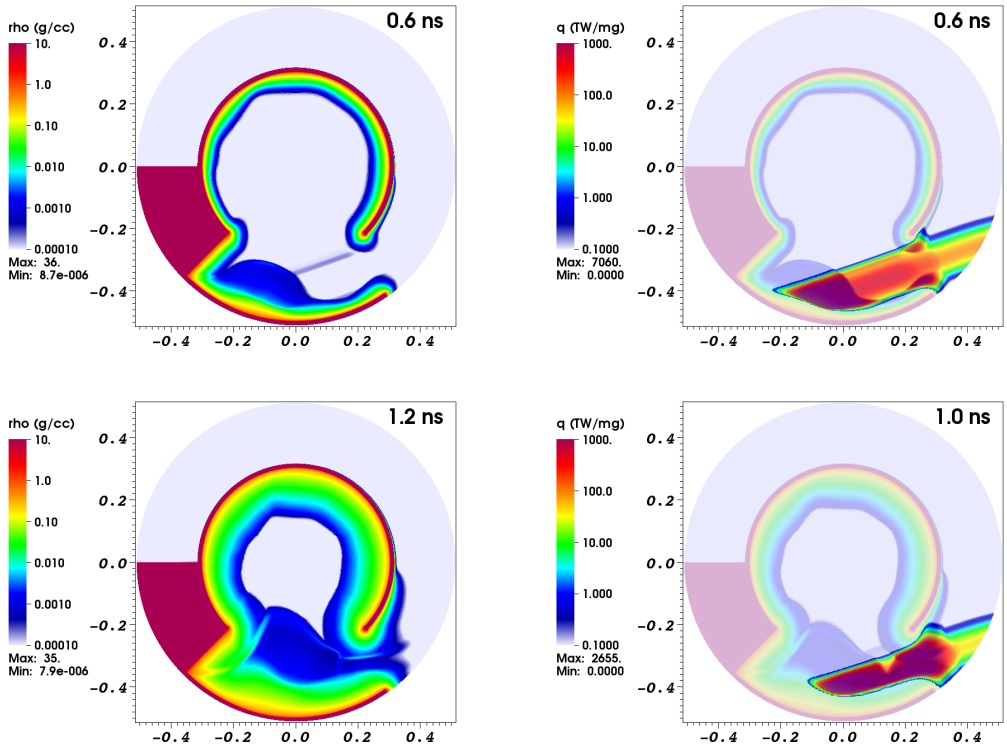

FIG. 3.19: Color contour plots of the plasma density ρ [g/cm^3] (left column), and of the mass-specific rate q [TW/mg] of the laser energy deposition (right column) in the empty Ω-hohlraum at two selected time moments.

and at the end ($t = 1.2$ ns) of the laser pulse. One sees that the plasma motion inside the secondary chamber of the Ω-hohlraum is significantly less violent than in the g1103 hohlraum of the same radius, where the laser beam entered the hohlraum chamber directly: by the end of the laser pulse $t = 1.2$ ns the ablated inner wall surface implodes by about 0.15 mm, i.e. by about half of the hohlraum radius; the central part of the secondary chamber remains virtually unperturbed by the plasma motion.

The last frame in the right-column of Fig. 3.19 demonstrates that a sufficiently efficient penetration of the laser beam into the primary hohlraum chamber is ensured down to the effective end of the laser pulse at $t = 1.05$ ns.

Of primary interest in the thermal history of the empty Ω-hohlraum is the peak value and the spatial uniformity of the radiation temperature T_r. The spatial uniformity of T_r in the secondary hohlraum chamber is illustrated by the two frames in the right-hand column of Fig. 3.20. One sees that, apart from the spurious ray effect, at $t = 0.6$ ns the radiation temperature inside the secondary chamber varies smoothly within the limits 85 eV $\lesssim T_r \lesssim$ 95 eV; by $t = 1.2$ ns this variation range becomes even more narrow, 75 eV $\lesssim T_r \lesssim$ 80 eV.

Similar to Fig. 2.10, Fig. 3.21 shows the temporal evolution of the average radiation, $T_{rc}(t)$, and matter, $T_c(t)$, temperatures near the center of the secondary chamber of the empty Ω-hohlraum. The peak value of the radiation temperature, reached at $t = 0.9$ ns, is $T_{rp} = 94$ eV, i.e. lies pretty close to the scaling law (2.12) for the single-chamber g1103 hohlraum, which yields $T_{rp} = 103$ eV for $E_{cyl} = 100$ J/mm. This comparison provides a

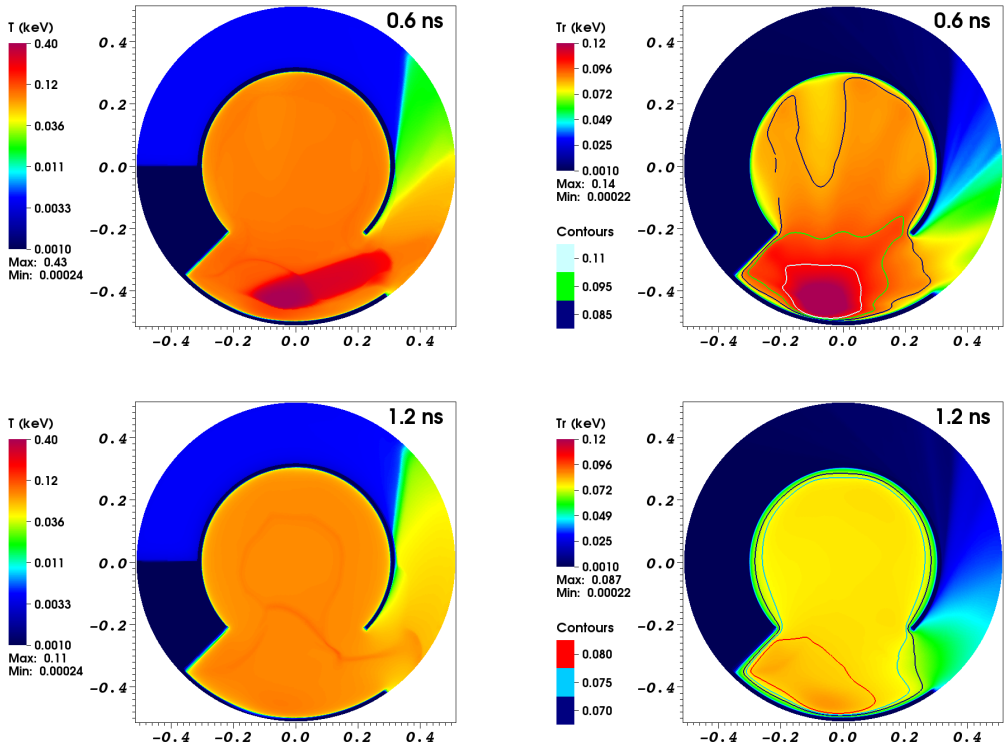

FIG. 3.20: Color contour plots of the matter temperature T [keV] (left column), and of the radiation temperature T_r [keV] (right column) in the empty Ω-hohlraum at two selected time moments.

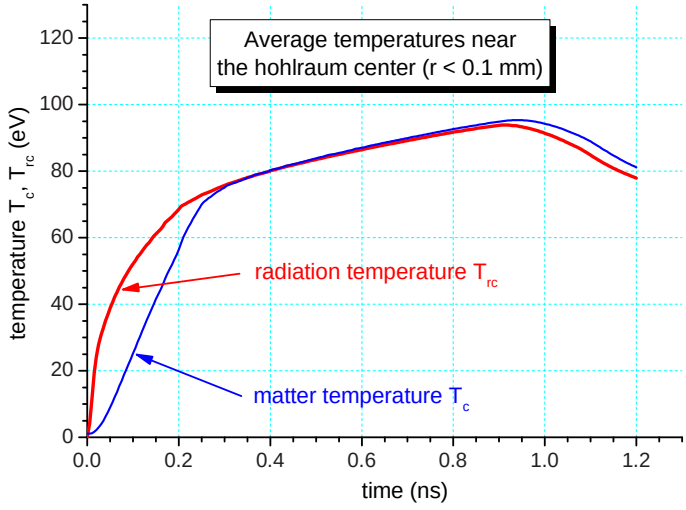

FIG. 3.21: Temporal evolution of the average matter and radiation temperatures near the center (at $r < 0.1$ mm) of the empty Ω-hohlraum.

quantitative measure for the relative efficiency of our two-chamber Ω-hohlraum with respect to the single-chamber g1103 hohlraum. As we see, introduction of an additional absorption chamber in the proposed hohlraum configuration leads to an $\simeq 10\%$ reduction of the hohlraum temperature.

3.3. Initial density of the carbon fill

We take pure carbon as a filling sample material for the secondary chamber of our Ω-hohlraum, and begin by evaluating its initial density from the energy balance considerations. Evidently, to reach carbon temperatures close to the peak temperature $T_{rp} = 94$ eV, registered in the empty Ω-hohlraum, the total energy, required to ionize and heat up the carbon mass M_C, must not exceed some reasonable fraction (say, 50%) of the total available energy $E_{cyl} = 100$ J/mm. As a consequence, we get the following inequality

$$\frac{1}{2}E_{cyl} > \frac{M_C}{Am_u}\left[\frac{3}{2}T(Z+1) + E_{iz}\right] \tag{3.22}$$

for tentative evaluation of the initial carbon density

$$\rho_{C0} = \frac{M_C}{\pi R_0^2}. \tag{3.23}$$

In Eq. (3.22) $A = 12$ and $Z = 6$ are, respectively, the atomic mass and the atomic number of carbon, m_u is the atomic mass unit, T is the desired temperature of the carbon plasma, $E_{iz} = 1030$ eV is the total energy of full ionization of the carbon atom. Having assumed the values $T \approx 100$ eV, $E_{cyl} = 100$ J/mm, $R_0 = 0.3$ mm, we obtain from Eqs. (3.22) and (3.23) an upper limit of

$$\rho_{C0} \lesssim 10 \ \text{mg/cm}^3 \tag{3.24}$$

for the initial carbon density ρ_{C0}. This limit implies that the hohlraum fill must be in the form of a low density foam. Below the results of simulation are presented for a three times lower initial carbon density of $\rho_{C0} = 3$ mg/cm^3.

3.4. Simulation results for a carbon-filled Ω-hohlraum

1. Initial state and simulation parameters

The initial configuration of the Ω-hohlraum, whose secondary chamber is filled with carbon at a density of $\rho_{C0} = 3 \times 10^{-3}$ g/cm^3, is shown in Fig. 3.22. All the dimensions are exactly as in Fig. 3.17. The 15-μm thick gold wall has the initial density of $\rho_{w0} = 18$ g/cm^3; its extension — the 15-μm thick circular layer of gold, separating the carbon fill from the primary hohlraum chamber, has the initial density of $\rho_{w1} = 3 \times 10^{-3}$ g/cm^3. The primary absorption chamber is filled with a gold vapor at a density $\rho_{v1} = 2 \times 10^{-4}$ g/cm^3. The vapor fill of the outer buffer zone has the density of $\rho_{v0} = 10^{-5}$ g/cm^3.

Because we now have two different materials in the computational domain and the interface between them has to be traced explicitly, the simulation was performed in the ALE mode (where every Lagrangian step is followed by an appropriate mesh rezoning) with the 1-st order Godunov scheme. When constructing the 2D mesh, the $0 \le \theta \le 2\pi$ range of the

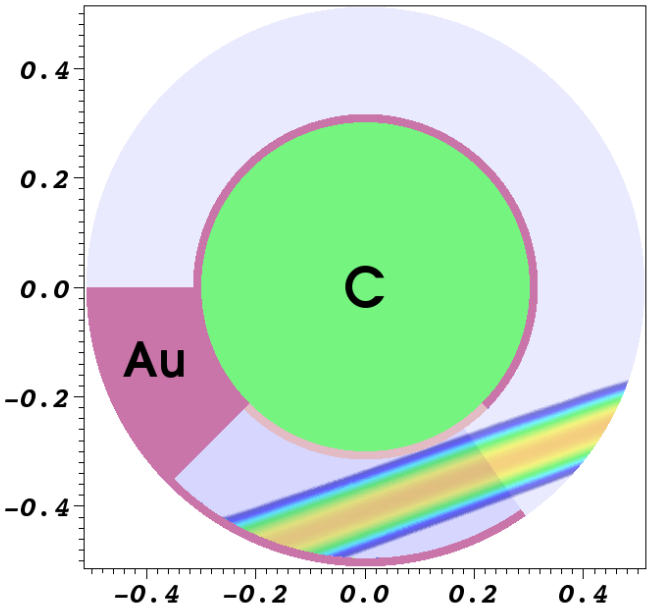

FIG. 3.22: Initial state of the computational region encompassing the carbon-filled Ω-hohlraum.

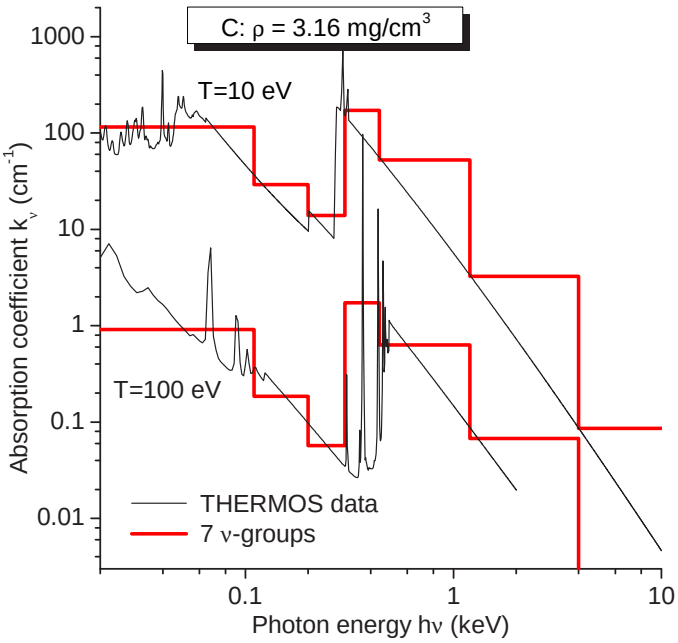

FIG. 3.23: Spectral absorption coefficient k_ν [cm^{-1}] of carbon at $\rho = 3.16 \times 10^{-3}$ g/cm^3 and two values of temperature: $T = 10$ eV and 100 eV. Shown are the original data from the THERMOS code (thin black curve) together with the group-averaged values for the 7 selected spectral groups (stepwise thick red curve).

polar angle θ was divided into 1080 uniform intervals (3 intervals per one degree of arc). On the total, the mesh consisted of 458 100 quadrilateral cells. Radiation transport coupled to hydrodynamics was simulated by using the S_{18} angular quadrature (360 ray directions over

the 4π solid angle) and the 7 frequency groups given by Eq. (3.21). The spectral dependence of the radiation absorption coefficient k_ν of carbon, used in the simulations, is shown in Fig. 3.23.

2. Simulation results

Figures 3.24 and 3.25 illustrate the hydrodynamics and the thermal history of the carbon-filled Ω-hohlraum. The four series of contour plots (each represented by four snapshots separated by 0.3 ns) display the temporal evolution and spatial distribution of the plasma density ρ, of the radiation, T_r, and matter, T, temperatures, and of the mean ionization degree z_{ion} during the laser pulse $0 < t < 1.2$ ns.

The contour plots of T and T_r show how the radiative heating wave propagates from the primary hohlraum chamber into the carbon foam during the initial heating phase $t \lesssim 0.7$ ns. At this phase the spatial distribution of the carbon temperature remains rather non-uniform: its variation across the secondary chamber amounts to several tens of electronvolts. The maximum temperature $T_{cp} \approx 90$ eV of carbon near the hohlraum center is reached by the end of the laser pulse at $t \approx 0.9$ ns. The detailed temporal evolution of the matter, $T_c(t)$, and radiation, $T_{rc}(t)$, temperatures near the hohlraum center (at $r < 0.1$ mm) is shown in Fig. 3.26.

By the end of the laser pulse the spatial uniformity of the carbon temperature significantly improves, and at 0.8 ns $\lesssim t \lesssim$ 1.3 ns its variation across the secondary hohlraum chamber is roughly ±5 eV. The radiation temperature T_r exhibits similar dynamics, although its spatial variation at all times is more smooth than that of T. A narrow local minimum of T_r near the upper end of the hohlraum cavity, clearly visible on the $t = 0.3$ ns frame in the right column of Fig. 3.24, has a spurious numerical origin due to the ray effect.

The four images on the right-hand side of Fig. 3.25 display the spatial distribution of the mean ionization degree z_{ion}. Similar to the matter temperature T, a fairly uniform distribution of the degree of carbon ionization $z_{ion} \approx 5.6$–5.8 is established across the carbon-filled chamber after $t = 0.8$ ns.

The uniformity of temperature distribution across the carbon fill is primarily controlled by its optical thickness with respect to the x-rays emerging from the laser absorption chamber. From Fig. 3.23 one infers that even in a relatively cold carbon plasma with $T \lesssim 10$ eV the mean free path of photons in a broad spectral range of $h\nu \approx 100$–350 eV amounts to $l_\nu = k_\nu^{-1} \approx 0.3$–$1$ mm, i.e. the optical thickness of the secondary chamber for these photons is $\lesssim 1$. As the carbon temperature rises and approaches 100 eV, the carbon-filled chamber becomes transparent for thermal x-rays over the entire spectrum. This is an important prerequisite for a uniform temperature distribution over the entire volume filled with carbon.

As one sees in the four frames of the left column in Fig. 3.24, the density of the carbon plasma over the most of its volume remains at its initial value 3×10^{-3} g/cm^3 — at least for $t \lesssim 1.2$ ns. However, the gold plasma, ablated from the inner surface of the dense hohlraum wall, drives a shock wave into the carbon fill, which converges towards the center of the secondary chamber. In Fig. 3.27 it is clearly seen how this shock compresses carbon from its initial density $\rho_{C0} = 3$ mg/cm^3 to $\rho_C \approx 8$ mg/cm^3 behind the front.

Clearly, propagation of the shock, driven by wall ablation, across the sample carbon plasma sets a limit on the time window within which one can count on a uniform plasma state of the sample material in the secondary chamber. In our case the inward bound shock front converges upon the center at $t \approx 3.5$ ns, as it is seen on the density and temperature

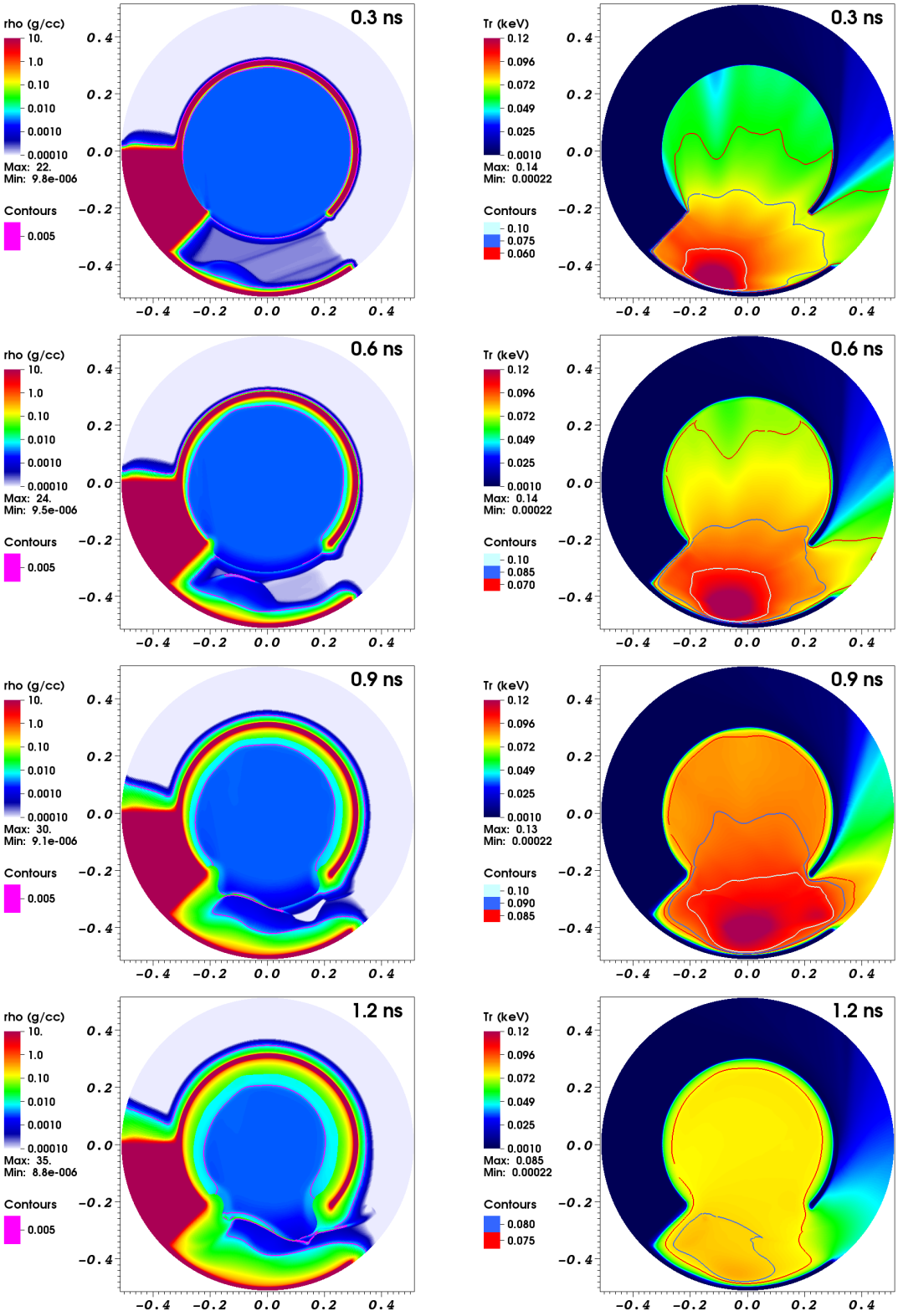

FIG. 3.24: Color contour plots of the plasma density ρ [g/cm^3] (left column) and of the radiation temperature T_r [keV] (right column) in the Ω-hohlraum with a 3-mg/cm^3 carbon fill at four selected times.

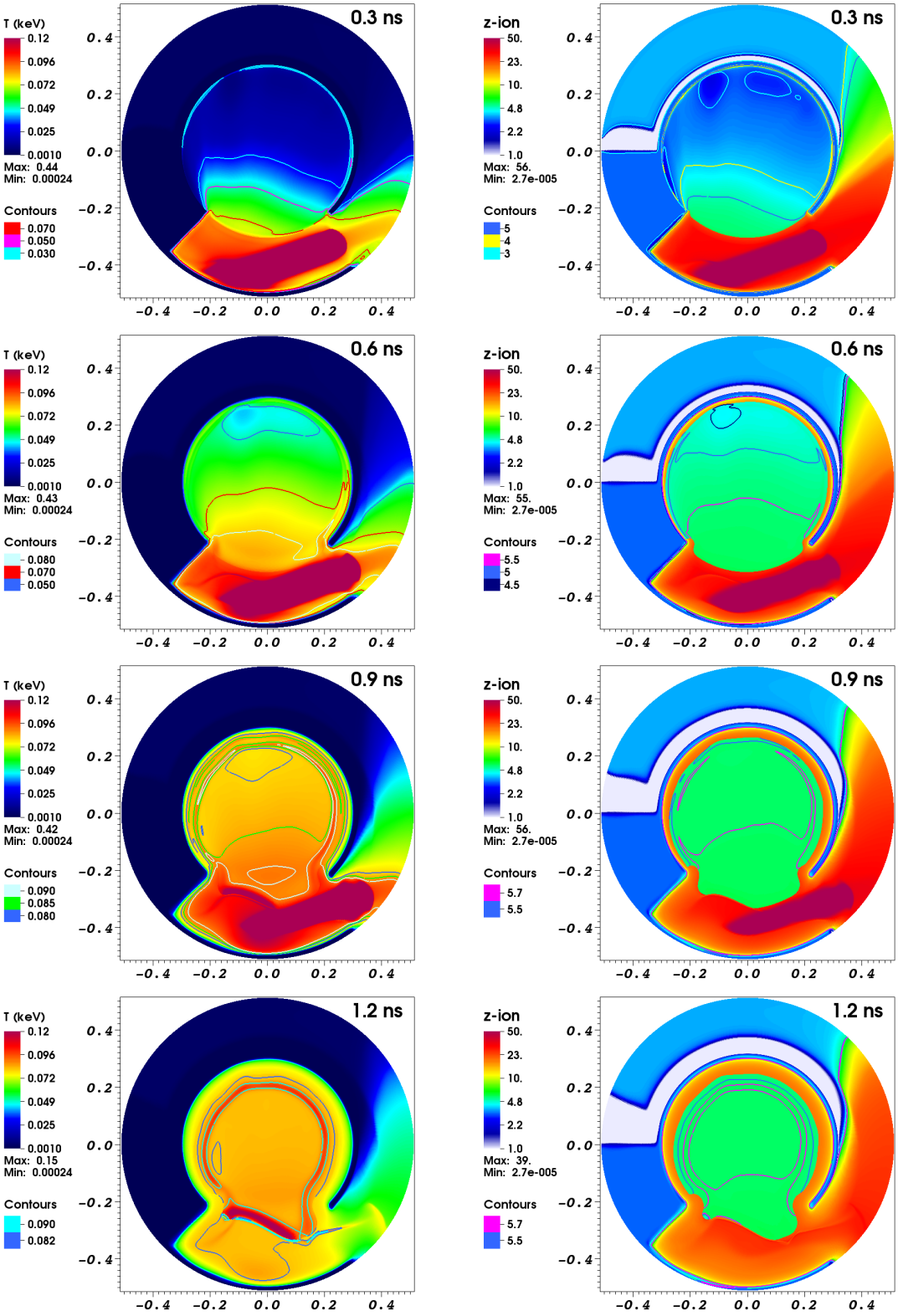

FIG. 3.25: Color contour plots of the matter temperature T [keV] (left column) and of the ionization degree z_{ion} (right column) in the Ω-hohlraum with a 3-mg/cm^3 carbon fill at four selected times.

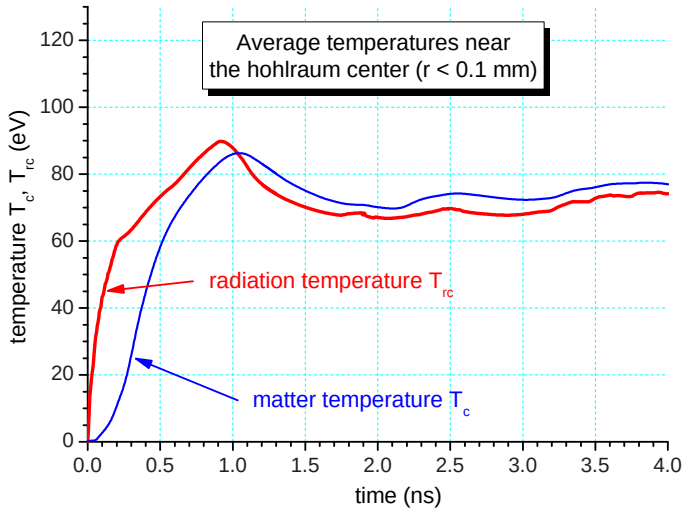

FIG. 3.26: Temporal evolution of the average matter and radiation temperatures near the center ($r < 0.1$ mm) of the Ω-hohlraum with a 3-mg/cm^3 carbon fill.

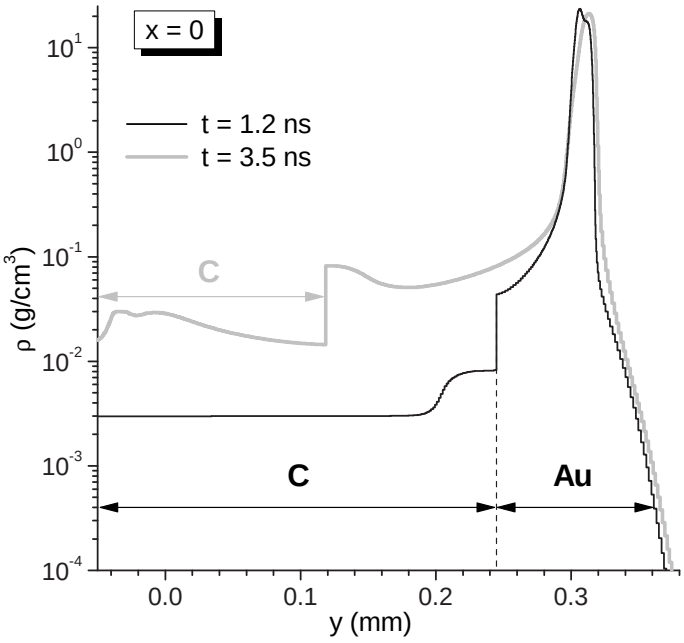

FIG. 3.27: Lineout plots of the plasma density ρ along the vertical line (i.e. along the y-coordinate) at $x = 0$ in the central part of the Ω-hohlraum for $t = 1.2$ ns and 3.5 ns.

color contour plots in Fig. 3.28. By this time, the radius of the carbon plasma shrinks to $r_C \approx 0.1$ mm (see Fig. 3.27).

Here, a special comment on the spurious effect of numerical diffusion would be in order. Having compared the density contour plots in the left-hand columns of Figs. 3.19 and 3.24, one notices that, whereas in Fig. 3.19 the upper part of the exterior hohlraum wall at $y > 0$ has a sharp edge (with the density jumping from 10^{-5} g/cm^3 in the outer buffer

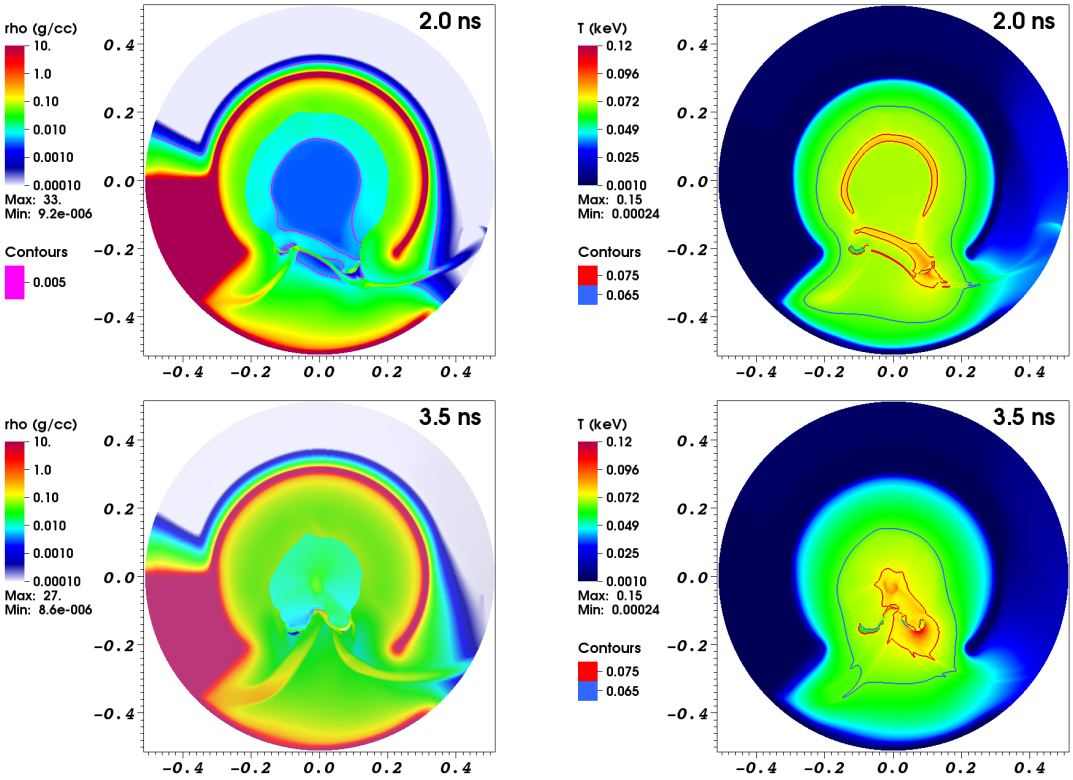

FIG. 3.28: Color contour plots of the plasma density ρ [g/cm^3] (left column) and of the matter temperature T [keV] (right column) in the Ω-hohlraum with a 3-mg/cm^3 carbon fill at $t = 2$ ns and 3.5 ns.

zone to 18 g/cm^3 in the solid gold), this same edge appears as rather fuzzy in Fig. 3.24. The 15 μm of solid gold is too much of a thickness for the perturbations from the inside of the hohlraum to reach its exterior surface: by $t = 1.2$ ns the outward bound shock front, launched by the hohlraum heating, covers only about 8 μm in solid gold. Thus, the fuzziness of the cold exterior hohlraum surface, observed in Fig. 3.24, is a pure numerical effect caused by significant diffusivity of the numerical scheme for remapping the principal physical quantities (mass, momentum and total energy) to a rezoned mesh in the ALE algorithm. Note that this type of numerical diffusion is absent in the pure Eulerian simulation presented in Fig. 3.19. The numerical diffusion is particularly strong in the first-order remapping scheme; the second-order algorithm was not used because in its present form it breaks down on too strong density jumps.

3.5. Conclusion

Summing up the above discussion of the simulation results, we conclude that in the present configuration a fairly uniform plasma state of practically fully ionized carbon with $\rho = 3 \times 10^{-3}$ g/cm^3 and 80 eV $< T <$ 90 eV can be created in the central region $r \leq 0.2$ mm of the secondary hohlraum chamber for a limited time interval of $\Delta t \approx 0.5$ ns, i.e. within the time window 0.8 ns $< t <$ 1.3 ns after the onset of the laser pulse with a total energy of $E_l = 100$ J/mm. If a quasi-uniform and a quasi-static plasma state of the sample material

must be ensured for a longer time interval, special measures should be taken in order to weaken the ablation-driven shock launched from the gold-carbon interface. To a ceratin degree, this could be achieved by optimizing the thickness and the initial density of the gold wall of the secondary chamber. However, a detailed investigation of this sort of dynamic confinement remains a topic for future work.

The present simulation was performed for a cylindrical Ω-hohlraum assumed to have infinite extension along the axial direction. In practice, however, the axial extension of the hohlraum would be limited to, probably, 1–2 mm. Then, if the ends of the cylindrical configuration are left open, the hot carbon plasma will flow out into vacuum through these ends. One readily evaluates that by $t = 1.0$–1.3 ns the width of the non-uniform unloaded zone at each end of the plasma column should not exceed $c_s t \approx 0.1$ mm, where $c_s \approx 9 \times 10^6$ cm/s is the sound speed in carbon at $T = 90$ eV. More difficult to evaluate is, of course, the additional radiation energy loss through the cylinder ends, which should bring down to a certain extent the maximum temperature reached in the carbon plasma. Clearly, the larger is the axial extension of the Ω-hohlraum, the smaller will be the relative effects of its ends.

Finally, it should be noted that if a significantly higher than $\rho_{C0} = 3 \times 10^{-3}$ g/cm^3 initial carbon density is chosen, the uniformity of the final temperature distribution in the sample plasma is essentially destroyed: when the same Ω-hohlraum was simulated with the initial carbon density of $\rho_{C0} = 10^{-2}$ g/cm^3, the spatial variation of the carbon temperature across the secondary hohlraum chamber at $t = 1.0$ ns was found to range from $T \approx 40$ eV at its far cold end to $T \approx 90$ eV near the hot primary chamber.

Acknowledgments

This work was supported by the ExtreMe Matter Institute EMMI in the framework of the Helmholtz Alliance Program HA216/EMMI.

APPENDIX A: APPROXIMATION OF 3D SPHERICAL HOHLRAUMS WITH PHYSICALLY EQUIVALENT 2D CONFIGURATIONS

When approximating the original 3D hohlraum with a "physically equivalent" 2D configuration, certain 3D parameters are to be rescaled to corresponding 2D values. We assume that two hohlraum configurations can be considered as physically equivalent when they have

(i) the same principal hohlraum radius R,

(ii) the same sizes (angular dimensions as viewed from the hohlraum center) of all holes, and

(iii) the same history of the hohlraum temperature $T_r = T_r(t)$.

Under these conditions one can expect that the hohlraum walls absorb approximately the same amount of energy per unit surface area and, as a consequence, exhibit similar dynamics of wall evaporation and hole closure. Then, the only parameter to be rescaled is the total input laser energy E (the normalized temporal profile of the input power is assumed to be

the same). The energy rescaling is performed by satisfying the following two equations of the global energy balance

$$E = F_w S_w + F_h S_h, \tag{A.1}$$
$$\tilde{E} = F_w \tilde{S}_w + F_h \tilde{S}_h. \tag{A.2}$$

Here E, S_w, and S_h are, respectively, the input energy, the total inner wall area, and the total inner hole area in the original 3D hohlraum configuration; $\tilde{E}$, $\tilde{S}_w$, and $\tilde{S}_h$ are the same quantities for the equivalent 2D configuration; F_w is the mean fluence (ergs/cm^2) of radiative energy absorbed by the inner surface of the hohlraum walls; F_h is the mean fluence (ergs/cm^2) of radiative energy escaping through the holes. For the same history of the hohlraum temperature $T_r(t)$, the area-specific quantities F_w and F_h can be assumed to be the same in both configurations. For a black-body spectrum of the hohlraum radiation, the quantity F_h can be evaluated as

$$F_h \approx \int \sigma_{SB} T_r^4 \, dt, \tag{A.3}$$

where σ_{SB} is the Stefan-Boltzmann constant.

Since the surface areas S_w, S_h, $\tilde{S}_w$, and $\tilde{S}_h$ are all known, Eqs. (A.1) and (A.2) yield the following expression for the rescaled input energy

$$\tilde{E} = E \, \frac{\tilde{S}_w + q_{hw} \tilde{S}_h}{S_w + q_{hw} S_h}, \tag{A.4}$$

where

$$q_{hw} = \frac{F_h}{F_w}. \tag{A.5}$$

The unknown dimensionless factor q_{hw} can be evaluated by successive approximations as follows. In the zeroth approximation one can assume that $F_h = F_w$, i.e. that $q_{hw} = q_{hw}^{(0)} = 1$, and perform a 2D simulation with

$$\tilde{E} = \tilde{E}^{(0)} = E \, \frac{\tilde{S}_w + \tilde{S}_h}{S_w + S_h}. \tag{A.6}$$

Making use of the results of this simulation, we can evaluate the first-order value of q_{hw} as

$$q_{hw}^{(1)} = \frac{\tilde{S}_w}{\tilde{S}_h} \frac{\tilde{E}_{r,out}^{(0)}}{\tilde{E}^{(0)} - \tilde{E}_{r,out}^{(0)}}, \tag{A.7}$$

where $\tilde{E}_{r,out}^{(0)}$ is the total amount of radiative energy, which escapes from the hohlraum in the zero-order 2D run. Equation (A.7) is a direct consequence of the global energy balance relation (A.2) combined with

$$\tilde{E}_{r,out} = F_h \tilde{S}_h. \tag{A.8}$$

Having substituted thus obtained value $q_{hw}^{(1)}$ into Eq. (A.4), we get a first-order estimate $\tilde{E}^{(1)}$ for the rescaled input energy $\tilde{E}$. Higher-order approximations are usually not needed.

Note that the factor q_{hw} can be expressed in terms of the mean wall albedo α_w, defined as

$$\alpha_w = \frac{F_h - F_w}{F_h} = 1 - \frac{1}{q_{hw}} < 1; \tag{A.9}$$

here F_h is the mean fluence of incident radiation energy, which in the first approximation is the same for the wall and hole surfaces; F_w is the mean energy fluence absorbed by the wall surface. Typical values for hohlraums with walls of a heavy metal are

$$\alpha_w \approx 0.3\text{–}0.5, \quad q_{hw} = \frac{1}{1-\alpha_w} \approx 2\text{–}3. \tag{A.10}$$

---

[1] E. Vasina, V. Vatulin, *Experimental Scheme for Investigation of Ion Stopping in Plasma – Indirect Laser Target Design*, GSI-200-2 Report, p. 52, 2000.

[2] M.M. Basko, An. Tauschwitz, J. Maruhn, *Development of a 2D radiation-hydrodynamics code RALEF for laser plasma simulations*, PLASMA-PHYSICS-25, GSI Report 2010-1 (GSI Scientific Report 2009), p. 410.

[3] D. Schumacher, A. Blazevic, A. Frank, T. Hessling, G. Schaumann, and M. Roth, *First hohlraum shots with the frequency doubled PHELIX laser beam*, PNI-PP-06, GSI Report 2011-1 (GSI Scientific Report 2010), p. 411.

[4] A. F. Nikiforov, V. G. Novikov, V. B. Uvarov, *Quantum-statistical models of hot dense matter: methods for computation of opacity and equation of state*, Birkhauser Verlag, Basel-Boston-Berlin, 2005.

[5] Ya. B. Zel'dovich and Yu. P. Raizer, *Physics of Shock-Waves and High-Temperature Hydrodynamic Phenomena. Vol. II.* (Academic Press, New York, 1967.)

[6] K.D. Lathrop, "Ray Effects in Discrete Ordinates Equations", Nucl. Sci. Eng., **32** (1968) 357.